**Helmholtz-Zentrum Dresden-Rossendorf (HZDR)**

# X-ray particle tracking velocimetry in liquid foam flow

Lappan, T.; Franz, A.; Schwab, H.; Kühn, U.; Eckert, S.; Eckert, K.; Heitkam, S.;

Perma-Link to Publication Repository of HZDR:

https://www.hzdr.de/publications/Publ-29866

# Soft Matter

# X-ray particle tracking velocimetry in liquid foam flow

Tobias Lappan[*a], Alexander Franz[b], Holger Schwab[c], Uta Kühn[c], Sven Eckert[a], Kerstin Eckert[ab] and Sascha Heitkam[*ab]

In this work, we introduce a novel approach to measure the flow velocity of liquid foam by tracking custom-tailored 3D-printed tracers in X-ray radiography. In contrast to optical observations of foam flow in flat cells, the measurement depth equals $100\,\text{mm}$ in X-ray beam direction. Light-weight tracers of millimetric size and tetrapod-inspired shape are additively manufactured from stainless steel powder by selective laser melting. Matching with the foam structure and bubble size, these tracers follow the foam flow minimally invasively. An X-ray beam passes through the radiotransparent foam channel and is detected by an X-ray image intensifier. The X-ray transmission images show the two-dimensional projections of the radiopaque tracers. Employing particle tracking velocimetry algorithms, the tracer trajectories are measured with both high spatial ($0.2\,\text{mm}$) and temporal ($25\,\text{fps}$) resolution. Fine-pored and coarse-pored liquid foam flow of different velocities are studied in a partly curved channel with rectangular cross section. The simultaneous time-resolved measurement of the tracers' translational motion and their intrinsic rotation reveal both the local velocity and vorticity of the foam flow. In the semi-circular curved channel section, the rigid-body-like foam flow pattern is investigated. Moreover, a relaxation of the foam structure in the transition zone between straight and curved section is observed.

## 1 Introduction

The mechanics of foam flow poses a complex and interesting academic problem since foam flow combines effects on several length scales. It incorporates rearrangement of the bubble structure, redistribution of contained liquid, lamella rupture, as well as sorption processes of surfactant molecules[1]. A better understanding of foam flow would allow to improve froth flotation[2], food production or processes in multi-phase reactors. Unfortunately, measurement techniques for foam flow are scarcely available because foam constitutes an opaque, complex and fragile composition of two or more phases.

The only measurement technique commonly used is optical observation of the surface of a foam sample, either at a free surface or close to a transparent wall[3–6]. Consequently, the few existing experiments regarding foam flow are usually done in Hele-Shaw cells, potentially biasing the flow behaviour[7]. By correlating subsequent images, velocity measurements are carried out with both high temporal and two-dimensional spatial resolution. At a transparent wall, the bubble size distribution and the local stress can be derived from the lamella size[8] and the deformation of the bub-

bles[9], respectively. In addition to optical observation, highly specialized bulk measurement methods with certain restrictions have been developed.

Magnetic resonance imaging, based on nuclear magnetic resonance, is capable of measuring the liquid fraction and also the motion of the liquid phase directly. However, individual measurements show high uncertainty, which results in measurement and averaging times of $90\,\text{s}$[10]. Consequently, only steady flows can be investigated.

Ultrasound Doppler velocimetry has been demonstrated to be applicable to medium scale foam flows[11]. Ultrasound pulses are sent into the foam and are reflected by air-water interfaces. The phase shift in the echo reveals the longitudinal velocity of the foam bulk along the beam axis. Due to the high attenuation of the ultrasound pulse in wet foam, the measurements are limited to very dry foam below $1\,\%$ liquid fraction. Employing an array of ultrasound transducers, the planar velocity field is resolved up to a measurement depth of $200\,\text{mm}$, which is approximately one order of magnitude larger than those of optical techniques.

Positron emission particle tracking allows for the tracking of radioactively marked tracer particles inside foam or froth with spatial resolution of approximately $1\,\text{mm}$ and velocities up to $1\,\text{m s}^{-1}$[12]. This technique has been used to observe the motion of lightweight hydrophobic particles and to conclude on the three-dimensional foam flow in model flotation cells. Combined with positron emission tomography, also the liquid fraction of foam

[a]Helmholtz-Zentrum Dresden-Rossendorf, Institute of Fluid Dynamics, 01328 Dresden, Germany. E-mail: t.lappan@hzdr.de, s.heitkam@hzdr.de
[b]Technische Universität Dresden, Institute of Process Engineering and Environmental Technology, 01062 Dresden, Germany
[c]Leibniz-IFW Dresden, Institute for Complex Materials, 01069 Dresden, Germany

is measurable[13]. However, the technique is restricted to a very low number of tracer particles in order to distinguish between them[14], which yields only point-wise measurements or long-term measurements in steady flow conditions.

X-ray tomography with synchrotron radiation has been used to generate tomographic images of the water structure in liquid foam around a spherical obstacle[15]. Tracking the evolution of this structure reveals the motion and gives insight into the local rearrangement mechanism in the foam. However, due to the low attenuation of X-ray in water only velocities below $1\,\mathrm{mm\,s^{-1}}$ and small measurement volumes can be achieved.

Neutron radiography has recently been employed for the first time to image liquid foam and particle-laden froth. Compared to X-ray imaging, water offers superior attenuation to neutron radiation, but the total flux density of neutrons is typically smaller than for X-ray photons. Neutron imaging is well-suited to measure the liquid fraction in the froth[16], to observe and track the foam structure, and to track particles in the froth which interact with neutrons[17].

To visualise and analyse the bulk flow of liquid foam, in this work we apply X-ray radiography based on custom-tailored tracers with both high spatial and temporal resolution. Particle tracking algorithms[18] are used to analyse the translational motion of the tracers as well as their intrinsic rotation within the foam flow. This novel method of X-ray particle tracking velocimetry (X-PTV) gives insight in the bulk flow field, but also the local vorticity of the foam structure. Calculating and comparing the velocities of the tracers' translational and rotational motion, we aim to show the rigid-body-like flow pattern of the liquid foam.

## 2 Experimental setup

### 2.1 Liquid foam flow

The foam flow experiments are performed inside an acrylic glass channel with a rectangular cross section of $30 \times 100\,\mathrm{mm^2}$ and 3 mm wall thickness (Fig. 1). A porous tube is placed at the bottom of the channel, submerged into surfactant solution. Charging the tube with compressed air, bubbles are injected continuously, generating a steady foam flow. The flow develops in the straight channel section, passes through the semi-circular curved channel section, and finally flows out into the open surrounding.

To prepare the surfactant solution, sodium dodecyl sulfate (SDS) is dissolved in deionized water. The surfactant concentration $c_{SDS}$ equals $0.1\,\mathrm{mol\,L^{-1}}$, which is one order of magnitude above its critical micelle concentration of $0.008\,\mathrm{mol\,L^{-1}}$[19]. This results in stable foam and a solution's surface tension $\sigma_b$ of $0.03\,\mathrm{N\,m^{-1}}$[20].

Two types of porous tubes with different pore size are used for bubble generation, yielding different bubble sizes. Evaluated optically in a pre-study, the bubble size $d_b$ ranges from 0.5 mm to 1.0 mm diameter for the fine-pored tube, and is monodispers with about 4.0 mm diameter for the coarse-pored one. The liquid fraction of the foam is estimated to be approximately 5 % and 1 %, respectively.

The bubble injection frequency and the thereby resulting foam flow velocity depends on the inlet air flow rate. It should be noted
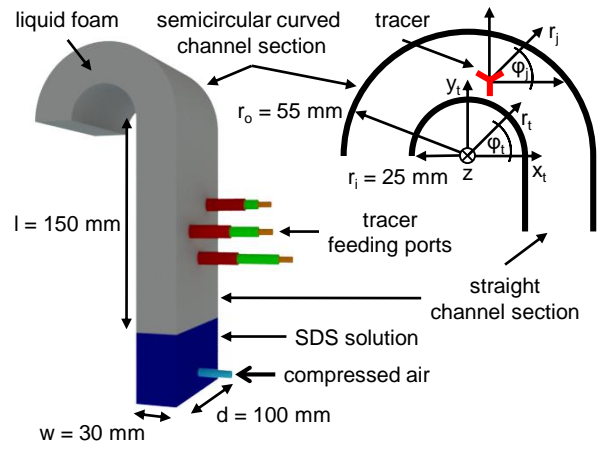


Fig. 1 Experimental setup: foaming and foam flow inside the channel, which is equipped for manual insertion of foam tracers.

that both porous tubes are supplied with the same constant pressure levels of compressed air, but have different pressure losses. Consequently, the velocity magnitude tends to be higher for the coarse-pored foam.

As listed in Table 1, six experimental parameter combinations of foam porosity and foam flow velocity are investigated. The initial flow velocity $v_0$ is measured and averaged in the region of interest close to the end of the straight channel section.

Table 1 Experimental parameter combinations: liquid foam porosity, bubble size and corresponding bulk flow velocity $v_0$

| foam porosity | fine-pored (fp) | coarse-pored (cp) |
|---|---|---|
| bubble size | 0.5 mm to 1.0 mm | $4.0\,\mathrm{mm} \pm 0.5\,\mathrm{mm}$ |
| fast flow (ff) | $7.8\,\mathrm{mm\,s^{-1}}$ | $26.0\,\mathrm{mm\,s^{-1}}$ |
| medium flow (mf) | $6.2\,\mathrm{mm\,s^{-1}}$ | $11.7\,\mathrm{mm\,s^{-1}}$ |
| slow flow (sf) | $3.2\,\mathrm{mm\,s^{-1}}$ | $4.5\,\mathrm{mm\,s^{-1}}$ |

The tracers are inserted manually into the foam flow. For this purpose, the straight channel section is equipped with three tracer feeding ports, allowing to choose the initial tracer position $x_0$ at the prescribed positions $y_0 = (-90\,\mathrm{mm}, -110\,\mathrm{mm}, -130\,\mathrm{mm})$ and $z_0 = (75\,\mathrm{mm}, 25\,\mathrm{mm}, 50\,\mathrm{mm})$. Since a maximum of three tracers can be fed in one measurement run in a well-controlled manner, several runs with identical foam parameters are combined to generate a relevant amount of trajectories.

### 2.2 Foam flow tracer

X-ray particle tracking velocimetry of liquid foam flow requires custom-tailored tracers fulfilling two basic criteria:

(i) The tracers follow the flow non-invasively.

(ii) The tracers are trackable in X-ray image sequences.

Criterium (ii) implies a sufficient X-ray image contrast between the tracer and the foam. Considering the measurement principle, the image contrast primarily depends on the difference between their X-ray attenuation coefficients $\mu_X^{tracer} \gg \mu_X^{foam}$. The X-ray attenuation, quantified by $\mu_X$, is a material-specific property correlating closely with the respective mass density $\rho$. Accordingly,

the tracers need to be made of some heavy metal instead of a light-weight polymer material. Even in case of iron, a material thickness of at least 0.1 mm is required to yield sufficient image contrast (see Section 3.1, Fig. 3). However, iron spheres with such diameter could not act as tracers. They would not follow the foam flow, but would drop through the foam Plateau borders due to gravity, violating criterion (i).

Our innovative solution to fulfil both criterion (i) and (ii), is the application of rod-based purposely shaped tracers to match with the foam structure and bubble size. Ideally, tetrapod-like shaped tracer easily stick to the Plateau borders and lamellae. CAD models of both such a rod-based (typ A1) and plate-based solid (type A2) are shown in Fig. 2a.

In this work, we have developed artificial tracers made of stainless steel 316L by selective laser melting (SLM). Since the three-dimensional solid structures are built up layer by layer, the tracer shape has to be modified according to the design guidelines for the additive manufacturing process, yielding three different 3D-printable tracer types. Inspired by a four-armed tetrapod, tracer type B consists of three plate-shaped parts with each 120° angle in between (Fig. 2b). Type C is similar, but weight-optimized (Fig. 2c). To minimize the tracer mass even further, the plate-shaped parts are shrunk to rod-like ones for type D (Fig. 2d).

The ability of these particles to follow the foam flow can be estimated considering a simplified bubble–tracer model. The distributed load $p_t$, resulting from the tracer's weight force, and the counteracting Laplace pressure $p_b$ on the surface of a single foam bubble are calculated as

$$\frac{m_t \cdot g}{A} = p_t < p_b = \frac{4 \cdot \sigma_b}{d_b} \tag{1}$$

with the tracer mass $m_t$, the gravitational acceleration $g$, the bubble–tracer effective contact surface area $A$, the bubble surface tension $\sigma_b$ and the bubble diameter $d_b$. The tracers weigh 0.015 g on average and have an effective contact surface area in the order of 10 mm², yielding 15 N mm⁻² distributed load. In comparison, the Laplace pressure equals 120 N mm⁻² to 240 N mm⁻² for the fine-pored foam, but only $p_b = 30$ N mm⁻² for the coarse-pored one. Consequently, fine-pored foam should easily carry the tracer while coarse-pored foam might yield limited ability for the tracer to follow the foam motion.

Despite the different tracer shape and weight, all tracer types B, C and D are used for the experiments to evaluate their performance under different foam flow conditions (Table 1).

## 3 Tracer particle tracking

### 3.1 X-ray transmission imaging
The measurement principle of X-ray transmission imaging is based on the material-dependent X-ray attenuation. In the first approximation, the Lambert-Beer law describes the X-ray transmittance $I/I_0$ as

$$\frac{I}{I_0} = \exp\left(-\mu_X \cdot d_z\right) \tag{2}$$

with the intensities $I_0$ and $I$ of the emitted and transmitted X-ray beam, respectively, the X-ray attenuation coefficient $\mu_X$ of the irradiated material and its thickness $d_z$ along the beam direc-

tion. Furthermore, attenuation coefficients are highly dependent on the X-ray photon energy $E_X$ [21].

In order to estimate the total X-ray transmission of the experimental setup (Fig. 1) and to predict the optimum X-ray photon energy, the following three components and their attenuation characteristics are considered (Fig. 3). First of all, the foam tracers need to be radiopaque and have a minimum X-ray transmittance, which is linked to employ as little X-ray photon energy as possible for imaging. Secondly and in contrast to the tracers, the liquid foam needs to be radiotransparent, meaning to have at least 80 % transmittance. Therefore, taking into account the foam channel depth $d = 100$ mm, X-rays with about 30 keV are required in case of the fine-pored foam flow. Due to the lower liquid fraction, $E_X \lesssim 20$ keV is sufficient for the coarse-pored foam. Additionally and as the third component, the foam channel walls contribute to the total X-ray transmittance of the experimental setup. Acrylic glass of 6 mm thickness in total decreases the initial X-ray beam intensity by approximately 20 % for $E_X = 30$ keV.

### 3.2 X-ray radiography setup
The foam flow experiments are imaged by means of an X-ray radiography setup (Fig. 4). Generated by the microfocus X-ray tube (XS225, Phoenix|X-ray), a horizontally aligned divergent X-ray beam passes through the 100 mm wide foam-filled channel and impinges on the input window of the X-ray image detector system. The X-ray image intensifier (TH9438HX, Thales) converts the transmitted X-rays into a two-dimensional visible light distribution, which is recorded by the CCD camera (CF8/1, Kappa).

To provide X-ray bremsstrahlung with maximum intensity at $E_X \approx 30$ keV, the X-ray imaging studies are performed using 45 kV tube voltage and 0.05 mA tube current. The field of view is centred on the semi-circular curved section of the foam channel, including the upper part of the straight section as well as the outlet, but not the tracer insertion zone, yielding 0.17 mm px⁻¹ image pixel size. The time-resolved X-ray image sequences are captured with a constant frame rate of 25 fps.

### 3.3 Image processing
The X-ray images show a depth-limited two-dimensional projection of the tracer-laden liquid foam flow in the acrylic glass channel. In order to compute the tracer velocities, the data analysis of the recorded images is divided into two subroutines. Firstly, the image series is pre-processed to detect each tracer. Secondly, both the tracer translational motion and the intrinsic rotation of the tracer around its centre position are tracked separately. The calculation of the respective velocities is described in Section 3.4.

The image pre-processing steps are illustrated in Fig. 5. Starting from the original 8-bit greyscale image (Fig. 5a), the tracers appear darker than the liquid foam, resulting from the higher X-ray attenuation of stainless steel compared to water. In consequence of the X-ray beam divergence, the acrylic glass channel walls aligned in beam direction are not projected as thin black lines, but rather appear as a dark grey areal projections. Therefore, the X-ray image contrast of tracers located close to the walls is reduced significantly. Applying colour inversion (Fig. 5b) and
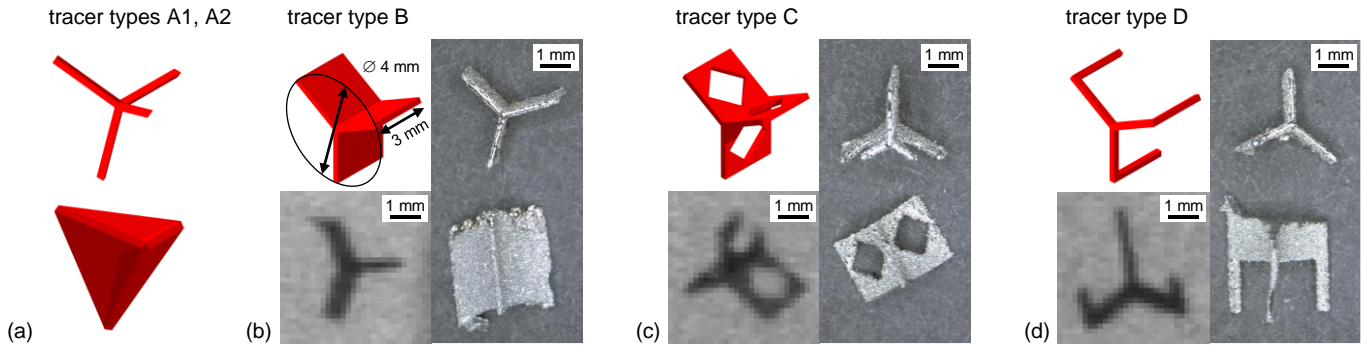
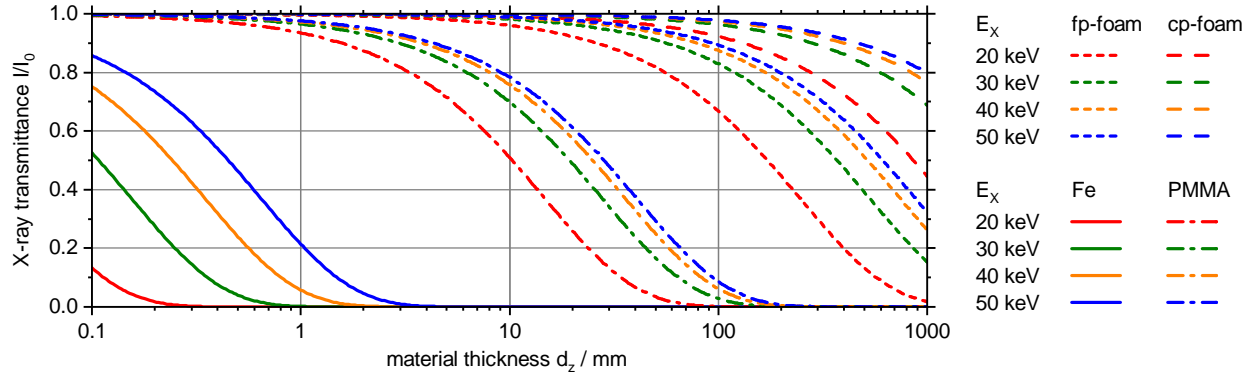Fig. 2 Foam flow tracer: CAD models, stereo-microscopic images and X-ray images of different tracer types.



Fig. 3 X-ray attenuation characteristics, calculated by Beer-Lambert law: X-ray transmittance $I/I_0$, depending on the irradiated material and its thickness $d_z$ along the X-ray beam direction.
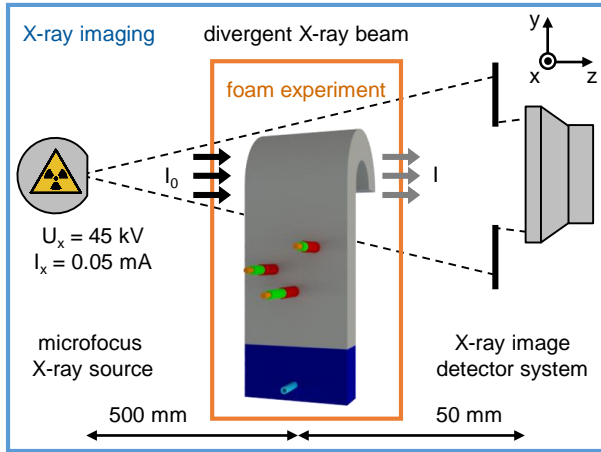


Fig. 4 Test arrangement for X-ray radiography of liquid foam flow.

subtraction of a time-averaged background image (Fig. 5c), the channel wall projections are removed and the tracers remain as the brightest objects within the image. However, the contrast level of each tracer projection still depends on its respective position. Subsequently, an edge detection algorithm is used to improve the image contrast by reconstructing the tracer shape (Fig. 5d). Finally, binarization by adaptive thresholding and outlier removal is applied, yielding a monochrome tracer shape image (Fig. 5e).

Proceeding from the pre-processed images, the tracking sub-routine is performed within the software Fuji and its plugin Track-Mate, employing blob detection based on the Laplacian of the Gaussian (LoG) and subsequent frame-to-frame linking by the Linear Assignment Problem (LAP) tracker[22]. For each image series, the blob detector is applied twice, but with different estimated blob diameter as the determining parameter. In the first step, to track the tracer translational motion following the streamlines of the foam flow, the diameter is set to 4.0 mm, corresponding to the average tracer size and thus covering the tracer projection entirely. In the second step, to track the tracer intrinsic rotation, the diameter is reduced to 1.0 mm, which is smaller than the tracer size. Hence, the blob detector recognizes only the edges of the tracer projection and characteristic structural features, like the three small rods of tracer type D.

Figure 6 exemplarily shows trajectories of the translational motion (labelled as *trans*) and the related intrinsic rotation (*rot1*, *rot2*, ...) of tracers with high and low ability to follow the foam motion, respectively. In the latter case, between $t_2$ and $t_3$ the tracer is not exclusively rotating around the $z$-axis and thus, the projected image is not only rotated, but the shape of the tracer projection changed suddenly within a few frames. Hence, the rotation tracking subroutine may provide inconsistent data, for example the trajectory *rot2* in Fig. 6b comes to an abrupt ending. However, the translation tracking is not affected significantly by such events. In general, the tracer's *trans*-trajectory and corresponding *rot*-trajectories do not cross, but run parallel to each other, indicating a rigid-body-like foam flow pattern.
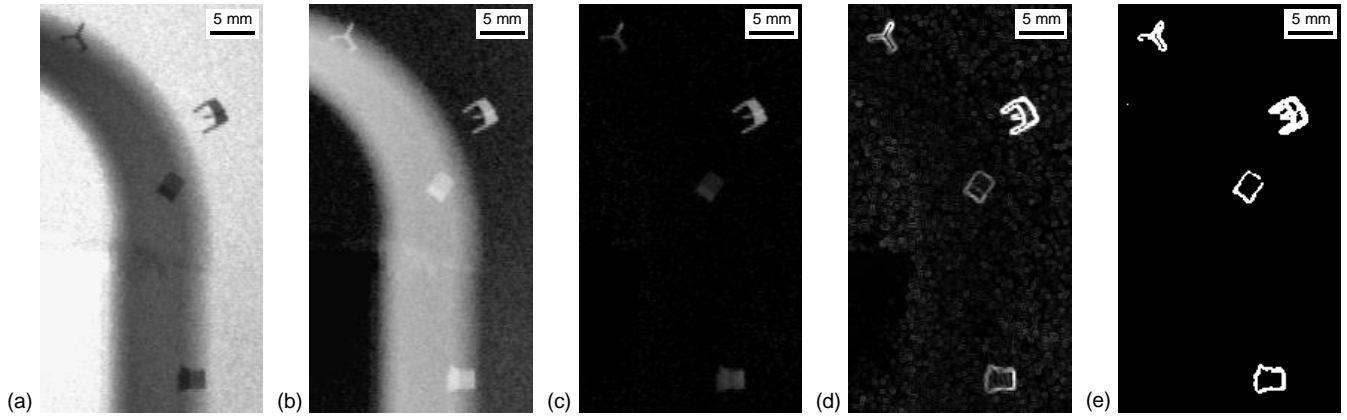
Fig. 5 Image pre-processing to detect the foam tracer: (a) original 8-bit greyscale image, (b) colour inversion, (c) subtraction of time-averaged background image, (d) tracer edge detection, (e) binarization by thresholding and outlier removal.
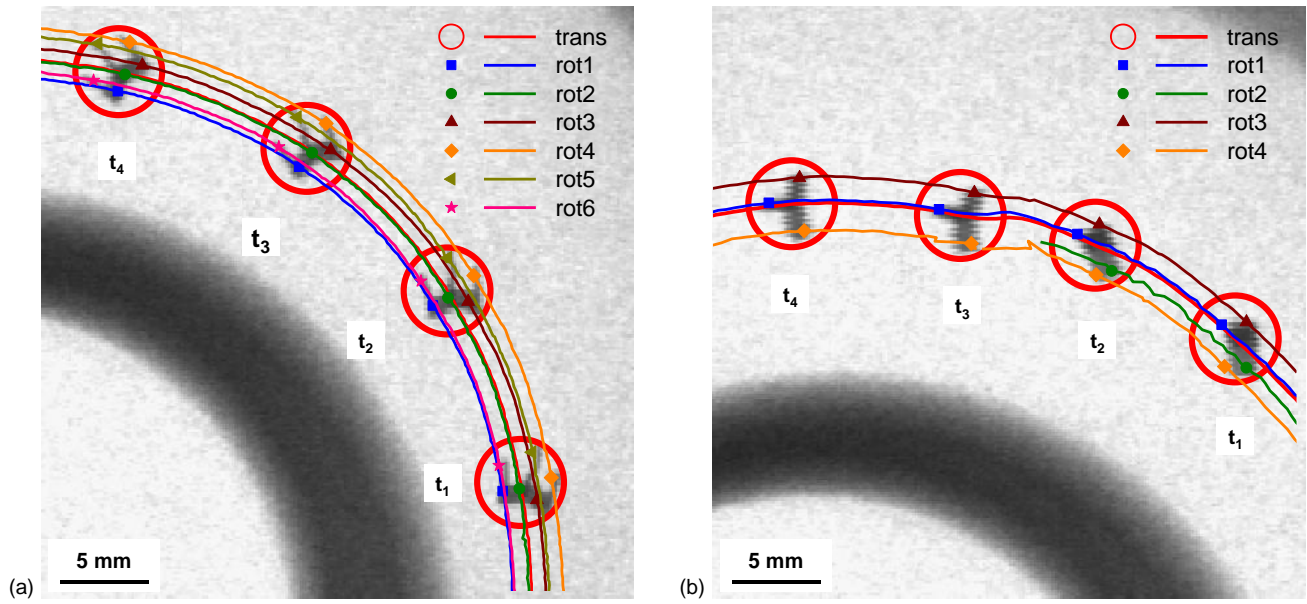


Fig. 6 Image processing to track both the tracer translational motion and the intrinsic rotation of the tracer around its centre position: (a) example of a tracer type D with *high* ability to follow the foam motion, (b) example of a tracer type B with *low* ability to follow the foam motion.

## 3.4 Trajectories and velocity calculation

For each tracer, both algorithms for translation and rotation tracking output results in the form of trajectories. Looking at each frame $i$, a trajectory consists of the respective position $\boldsymbol{X}^i$ and the corresponding velocity $\boldsymbol{U}^i = (\boldsymbol{X}^{i+1} - \boldsymbol{X}^{i-1})/(2\Delta t)$, calculated from central differencing scheme with $\Delta t = 0.04\,\mathrm{s}$ time increment.

The translational motion of the tracer centres is described by the variables $\boldsymbol{X}_t = (x_t, y_t)$ with the initial bulk flow velocity $v_0$. Focussing on the semi-circular curved channel section, the Cartesian coordinates $(x_t, y_t)$ are transformed to the polar coordinates $(r_t, \varphi_t)$, and the velocity components $(\dot{x}_t, \dot{y}_t)$ to $(\dot{r}_t, \omega_t)$. Savitzky-Golay filtering[23] by a 25-point cubic polynomial is applied to smooth the tracer velocity data. This filter preserves local velocity minima and maxima, which could indicate deviations between the motion of tracers and foam.

The intrinsic rotation of each tracer is revealed by set of $j = 1 \ldots n$ trajectories $\boldsymbol{X}_r^i = \{\boldsymbol{X}_1^i, \boldsymbol{X}_2^i, \ldots, \boldsymbol{X}_n^i\}$ in each frame $i$ (see Fig. 6). These trajectories correspond to the movement of cer-

tain structural features of the tracers. Their motion relative to the tracer centre is linked to the tracer rotation. Hence, they are analysed within the Lagrangian frame of reference following the translational motion of the respective tracer's centre. Therefore, the rotation trajectories are transformed to a polar coordinate system, whose origin of coordinates moves with $\boldsymbol{X}_t^i$, and described with $\boldsymbol{X}_j^i = (r_j^i, \varphi_j^i)$. If the radius $r_j^i$ is smaller than the estimated tracer size of $4.0\,\mathrm{mm}$, this structural feature is considered to be attached to the corresponding tracer centre. The average rotational angle $\varphi_r^i$ then is computed by averaging over all corresponding $\varphi_j^i$ with $r_j^i < 4.0\,\mathrm{mm}$ and applying a central moving average filter with a window length of 25. The rotational velocity of a tracer $\omega_r = (\varphi_r^{i+1} - \varphi_r^i)/\Delta t$ is derived by a differencing scheme with $\Delta t = 0.04\,\mathrm{s}$ time increment.

Depending on the tracer's position in radial ($r_t$) and angular direction ($\varphi_t$) in the semi-circular curved channel section, the angular velocity $\omega_t$ of the translational motion as well as the rotational velocity $\omega_r$ of their intrinsic rotation are analysed.

# 4 Results

## 4.1 Expected foam flow regimes

The liquid foam moves as plug flow with constant velocity $v_0$ in the straight channel section. Entering the curved section, the foam moves along semi-circular path. In general, two different flow shapes are conceivably, either with constant velocity $v_\varphi$ equal to $v_0$ or with constant angular velocity $\omega_t$ (see Fig. 7). The subindex $()_t$ characterises the variables describing the tracers' translational motion (see Section 3.4).

Case 1 would be a movement similar to a rigid-body rotation. In that case, the angular velocity $\omega_t$ would be constant, i.e. independent from the radial position $r_t$.

$$\omega_t(r_t) = \text{const.} \tag{3}$$

$$v_\varphi(r_t) = v_0 \cdot \frac{2 \cdot r_t}{r_i + r_o} = \omega_t \cdot r_t \tag{4}$$

The theoretical intrinsic tracer rotation is given by the rotation of the velocity field $\boldsymbol{u}$.

$$\omega_r = \frac{1}{2}(\nabla \times \boldsymbol{u})\boldsymbol{e}_z = \omega_t \tag{5}$$

In Case 1, the foam flow has to decelerate (for $r_t \lesssim (r_i + r_o)/2$) and accelerate (for $r_t \gtrsim (r_i + r_o)/2$) suddenly at the transition from the straight to the curved channel section. To fulfil the conservation of volume, also a radial displacement $\Delta r$ of the foam has to take place, as depicted in Fig. 7. The displacement can be calculated by employing the conversation of volume in horizontal slices. At the inner ($r_i$) and outer wall ($r_o$), the displacement equals zero.

$$v_0 \cdot (\tilde{r} - r_i) = \int_{r_i}^{\tilde{r} + \Delta r} \omega_t \cdot r_t \, dr_t \tag{6}$$

$$\Delta r(\tilde{r}) = \sqrt{(r_i + r_o)(\tilde{r} - r_i) + r_i^2} - \tilde{r} \tag{7}$$

Case 2 for the velocity distribution in the curved channel section would be a constant velocity. Consequently, the angular velocity would scale $\omega_t \propto 1/r_t$, yielding the theoretical intrinsic tracer rotation $\omega_r$ in Eq. (9). This case would be linked to a steady shear rate of the foam in the curved section.

$$v_\varphi(r_t) = v_0 = \text{const.} = \omega_t \cdot r_t \tag{8}$$

$$\omega_r = \frac{1}{2}(\nabla \times \boldsymbol{u})\boldsymbol{e}_z = \frac{1}{2}\frac{v_0}{r_t} = \frac{1}{2}\omega_t \tag{9}$$

To distuinguish between Case 1 and Case 2, the intrinsic tracer rotation $\omega_r$ is normalized with the angular velocity, yielding the velocity ratio $k_\omega$ between the angular and rotational velocity.

$$k_\omega = \omega_r/\omega_t \tag{10}$$

In case of solid-body rotation, $k_\omega$ equals 1.0. In the other case of constant-velocity flow, $k_\omega$ equals 0.5.

In the following, the quantities $\omega_t$, $\Delta r$ and $k_\omega$ are analysed and discussed depending on the tracer's radial position $r_t$.
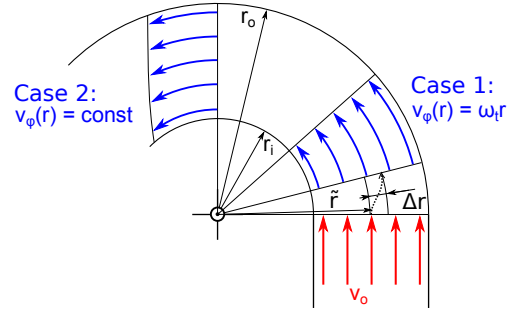


Fig. 7 Visualisation of two possible flow cases in the semi-circular curved channel section and explanation for the radial displacement $\Delta r$ when switching from plug flow to solid-body rotation.

## 4.2 Tracer translational motion: trajectories

The trajectories of the tracer translational motion with the fine-pored and coarse-pored foam flow are shown in Fig. 8. An array of trajectories, containing a number of approximately 50 tracers, is recorded for the respective parameter combination of foam porosity and initial flow velocity. Due to three different insertion positions $x_0 = \{30\,\text{mm}, 40\,\text{mm}, 50\,\text{mm}\}$ in the straight channel section, the trajectories cover the whole channel width, ranging from the inner radius $r_i = 25\,\text{mm}$ to the outer radius $r_o = 55\,\text{mm}$ in the semi-circular curved channel section. After passing the channel outlet, the tracers seem to move unaligned, since the liquid foam flow outside the channel differs significantly between consecutive runs. The tracer position in $z$-direction along the X-ray beam is not considered.

In general, the trajectories run parallel to each other and follow the channel curvature smoothly, indicating that the tracers followed the laminar flow very well. However, a few trajectories show a step-like translational motion in negative radial direction ($\dot{r}_t < 0$) and thus, deviate from the foam flow streamlines locally. Such a tracer behaviour is observed particularly in coarse-pored foam and becomes significantly more distinct with increasing flow velocity. The interdependence between foam flow and tracers will be discussed in Section 5.

## 4.3 Tracer translational motion: angular velocity

In the semi-circular curved channel section, the tracers move along semi-circular paths. Therefore, the angular velocity $\omega_t$ is analysed, depending on the radius $r_t$, for various angle $\varphi_t$. Each data point in Fig. 9 corresponds to one tracer and its respective position $(r_t, \varphi_t)$. For the further analysis, the measurement data from several runs are combined with respect to the foam porosity (fp, cp) and the initial flow velocity (ff, mf, sf) (see Table 1). Each data series is fitted by a linear regression, yielding the graphs shown in Fig. 9 and the corresponding slopes $m_{\omega_t} = \partial \omega_t / \partial r_t$ listed in Table 2. Within the semi-circular curved channel section ($\varphi_t = \{0.25\pi, 0.5\pi, 0.75\pi\}$), $m_{\omega_t}$ has values close to zero. In a few cases, at the section's beginning ($\varphi_t = 0$) and ending ($\varphi_t = \pi$) as well as for the cp-ff data, $m_{\omega_t}$ describes the significant reduction of $\omega_t$ with increasing $r_t$.

Afterwards, $\omega_t$ is again analysed for all $\varphi_t = [0, \pi]$, but independently from $r_t$. Figure 10 shows the mean angular velocity
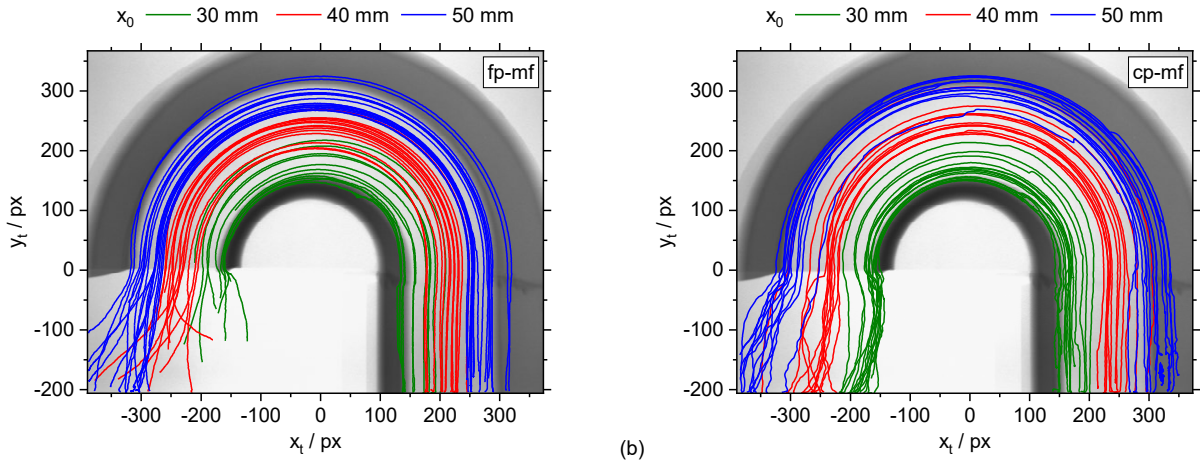
Fig. 8 Tracer translational motion (a) with the fine-pored and (b) with the coarse-pored foam moving with medium velocity: the trajectories, depending on the tracer insertion position $x_0$, cover the inner, middle and outer radius range in the semicircular curved channel section. The foam channel's projection, imaged by the divergent X-ray beam, is shown in the background.

Table 2 Angular velocity $\omega_t$, depending on the radius $r_t$ of the tracer trajectories at various angle $\varphi_t$: linear-fitted slope $m_{\omega_t}$ / $10^{-4}\,\mathrm{rad\,s^{-1}\,mm^{-1}}$

| $\varphi_t$/rad | fp-ff | fp-mf | fp-sf | cp-ff | cp-mf | cp-sf |
|---|---|---|---|---|---|---|
| 0 | -34 | -28 | -7 | -114 | -41 | -16 |
| $1/4\,\pi$ | 5 | -6 | 3 | -67 | 1 | -5 |
| $1/2\,\pi$ | 1 | -5 | 1 | -55 | -13 | 1 |
| $3/4\,\pi$ | 3 | -8 | -1 | -63 | -8 | 3 |
| $\pi$ | -23 | -32 | -17 | -179 | -92 | -27 |

$\overline{\omega_t}(\varphi_t)$, averaged for each angle $\varphi_t$ ($r_t = [25\,\mathrm{mm}, 55\,\mathrm{mm}]$), and the corresponding standard error of the mean. In good approximation, $\overline{\omega_t}$ either remains at a constant level (fp-mf/sf, cp-mf/sf) or is slightly increasing (fp-ff, cp-ff), while the foam flow passed through the semi-circular curved channel section. Near its beginning ($0 \lesssim \varphi_t \lesssim \pi/6$) and ending ($5/6\pi \lesssim \varphi_t \lesssim \pi$), the largest deviations from the mean are observed.

Finally, in order to analyse the tracer translational motion in the transition zone between both channel sections, all data for fine-pored and coarse-pored foam flow, respectively, are combined. The radial displacement $\Delta r_t$ of each tracer in the transition between straight and curved section is shown in Fig. 11. The data are subjected to high uncertainty because the detection of the absolute radial position is biased by the divergence of the X-ray beam. Also, the displacement depends on the definition of start and end position along the trajectory. In Fig. 11, the start position is below the channel transition ($y_t = -20\,\mathrm{mm}$) and the end position is at $\varphi_t = \pi/4$, where Fig. 9 suggests a developed flow. Despite the uncertainty, a clear trend for positive radial displacement in the centre of the channel and a rough agreement to the theoretical estimation in Eq. (7) are visible.

### 4.4 Tracer intrinsic rotation: rotational velocity

Besides the tracer translational motion and its constant angular velocity $\omega_t$, evaluated in the semi-circular curved channel section, the velocity $\omega_r$ of the tracer intrinsic rotation is analysed. Hypothesising that the intrinsic rotation is closely linked to the translational motion, as observed in Fig. 6, the velocity ratio $k_\omega = \omega_r/\omega_t$

is introduced. Figure 12 shows the mean value of $k_\omega$, depending on the radius $r_t$. Each data point corresponds to one or more tracers moving at a certain $r_t$ in the angular range $\pi/4 \leq \varphi_t \leq 3\pi/4$. The error bars represent the standard error of the mean. Except for the coarse-pored fast-flowing foam, the angular velocity and the intrinsic rotational velocity have a similar magnitude, yielding an approximately constant velocity ratio $k_\omega \simeq 1.0$.

## 5 Discussion

The measured quantities allow to distinguish between solid-body rotation (Eq. (3)) and constant-velocity flow (Eq. (8)) in the semi-circular curved channel section.

The angular velocity $\omega_t$ in Fig. 9 demonstrates, that inside the curved channel in case of fine-pored foam flow as well as coarse-pored foam flow with low or medium velocity, a rigid-body-like movement is present, because the angular velocity is nearly independent from the radial position. This is in line with the velocity ratio $k_\omega$ in Fig. 12, showing values close to 1.0 for these cases. Finally, the measured radial displacement in Fig. 11 coincides with the predicted displacement in Eq. (7).

However, fast-flowing coarse-pored foam has a tendency towards the constant-velocity case. The angular velocity $\omega_t$ decreases with increasing radius $r_t$ (see Fig. 9f-j). The reason for the different velocity field in case of coarse-pored foam moving at high velocity could be, that the comparatively higher friction at the channel side walls tends to balance the velocity over the cross section. At the same time, the lower yield stress of the coarse-pored foam allows steady shear strain to take place.

The velocity ratio $k_\omega$ in case of fast-flowing coarse-pored foam does not support the tendency towards the constant-velocity case. Figure 12d does not show values significantly lower than 1.0, but large fluctuations. Presumably, the comparatively high shearing rate of the foam causes dropping events of the foam tracers, because shearing is linked to local rearrangement of the bubble structure. If such rearrangement took place in the vicinity of a tracer, the intermediate stages do not provide minimum-energy positions for the tracer and consequently, it drops.
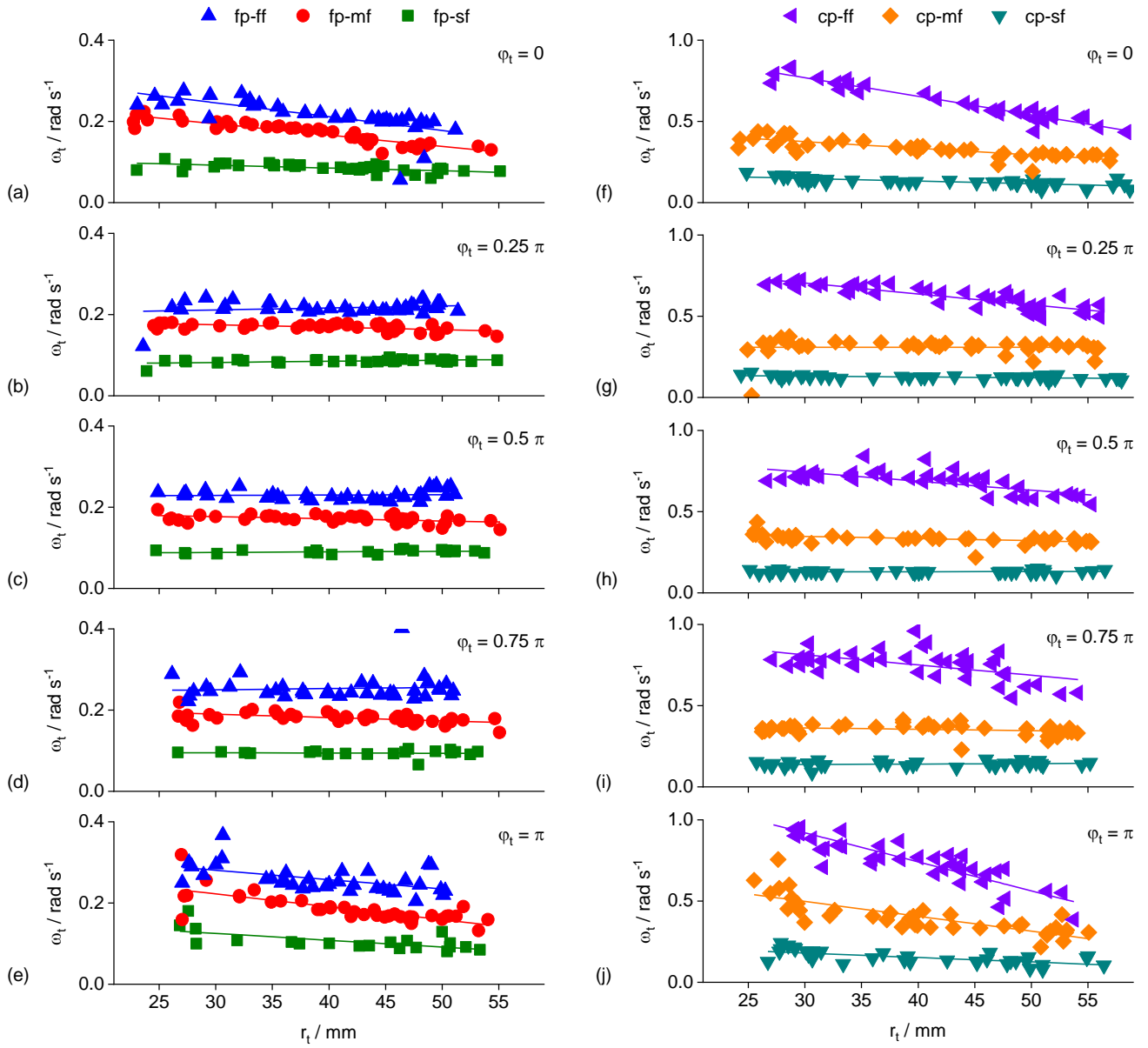
Fig. 9 Tracer translational motion (a)-(e) in the fine-pored and (f)-(j) in the coarse-pored foam flow in the semi-circular curved channel section: angular velocity $\omega_t$, depending on the radius $r_t$, at various angular positions $\varphi_t$.
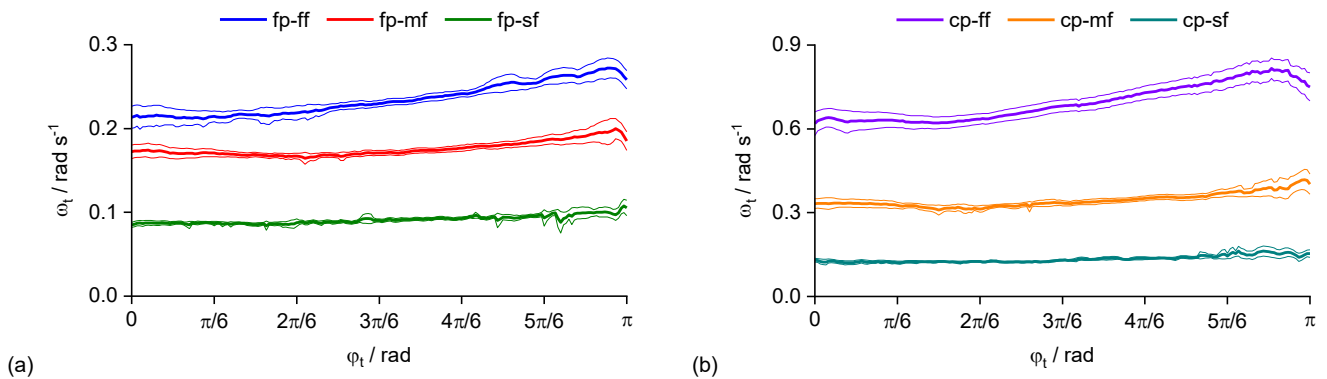


Fig. 10 Tracer translational motion (a) with the fine-pored and (b) with the coarse-pored foam flow in the semi-circular curved channel section: angular velocity $\omega_t$, averaged over the radius $r_t$, depending on the angle $\varphi_t$.
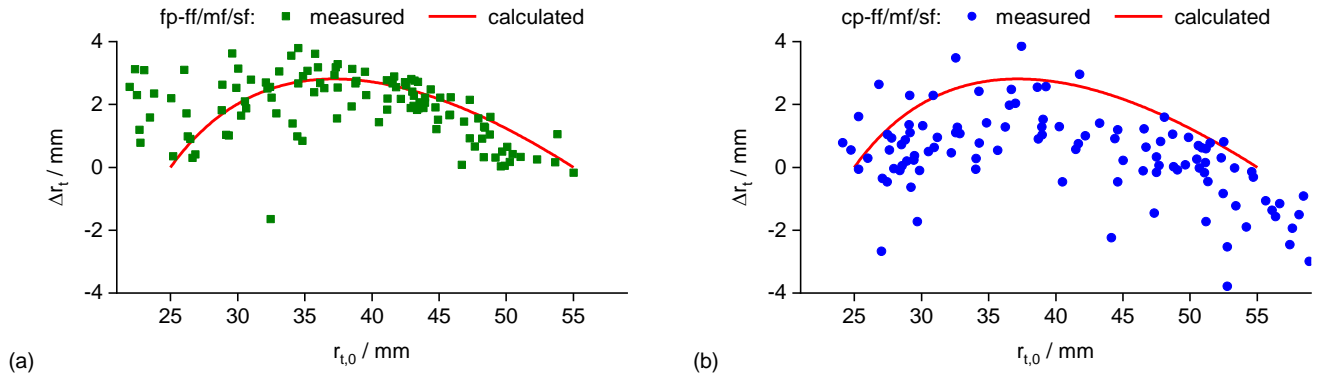
Fig. 11 Radial displacement during the tracer translational motion (a) with the fine-pored and (b) with the coarse-pored foam flow from the straight into the semi-circular curved channel section. The solid line indicates the theoretical displacement according to Eq. (7).

The three foam tracer types used for these imaging studies perform slightly differently. On the one hand, all kinds of tracers stick and float nearly perfectly with the fine-pored foam flow. On the other hand, tracers with plate-shape structure (types B, C) tend to be too heavy to follow the coarse-pored foam flow in all circumstances. In individual cases, the tracer weight force triggers either film rupture or bubble rearrangement and thus, biases the foam flow locally. These events yield step-like trajectories. The data analysis of the tracer translational motion works out robust, but fails to calculate the intrinsic rotation during such events. Consequently, the measurements on fast-flowing coarse-pored foam are fraught with comparatively higher uncertainty.

The tracer dimensions of 3 mm to 4 mm equal the foam bubble size of approximately 4 mm in the coarse-pored foam. Therefore, the tracer intrinsic rotation results from the local velocity gradient between a pair of neighbouring foam bubbles. In contrast, the misfit between this tracer size and the smaller bubbles of maximum 1 mm diameter in the fine-pored foam limits the spatial resolution to larger bubble clusters.

To optimize the X-ray image contrast between the radiopaque tracers and the radiotransparent liquid foam, the X-ray tube voltage and current need to be adjusted during the measurements. Because of the slightly different liquid fraction, fine-pored foam is less radiotransparent than coarse-pored one under otherwise identical imaging conditions. Additionally, the intensity of the transmitted X-ray beam is further decreased by the acrylic glass channel. Particularly the channel walls aligned in X-ray beam direction are imaged as two-dimensional areal projections due to the beam divergence, yielding a significantly reduced image contrast for tracers located close to these walls.

Systematic measurement uncertainties arise from the X-ray beam divergence, and impinge upon the tracer projection size and the radial position $r_t$ in the semi-circular curved channel section. The X-ray image pixel size of $0.17\,\mathrm{mm\,px^{-1}}$ refers to the reference plane, which is defined in the foam channel's centre ($z = 50\,\mathrm{mm}$) in beam direction. Projections of tracer located in front of this plane are enlarged and shifted in positive radial direction, whereas the size and the radial position of tracers closer to the detector plane are systematically undervalued. However, both the angular and rotational velocity are not affected by the

propagation of these uncertainties, since they rely on the ratio of certain distances in the image. Furthermore, if tracer size and shape would be more exact, the beam divergence could give rise to a three-dimensional tracking by analysing and comparing the tracer projection with the actual tracer size.

## 6   Conclusions

In this work, we present the first application of 2D X-ray radiography to image liquid foam flow employing 3D-printed custom-tailored tracers. The method allows to track the tracers inside the foam-filled channel of $100\,\mathrm{mm} \times 100\,\mathrm{mm}$ cross section. The measurement principle is based on the strong X-ray attenuation of the metallic tracers, yielding two-dimensional tracer projections. Both the tracers' translational motion and their intrinsic rotation are analysed, revealing a rigid-body-like flow of the liquid foam.

In particle tracking velocimetry, individual tracer particles, having low inertia to follow the fluid motion optimally, are tracked over time to conclude on the fluid velocity. For our method, we have developed foam tracers with a tetrapod-inspired shape, which are manufactured from stainless steel by selective laser melting. Besides the foam flow velocity, the unique three-dimensional shape allows to track the tracer intrinsic rotation and thus, to gain additional information on the local vorticity of the foam structure.

X-ray particle tracking velocimetry gives a detailed insight into the bulk flow of liquid foam, but with certain restrictions. On the one hand, due to the measurement principle of X-ray attenuation, X-ray radiography provides only depth-limited two-dimensional projection images. On the other hand, the foam flow could be biased by the light-weight but comparatively large tracers. However, X-PTV offers unique measurement possibilities compared to optical or other radiation-based measurements techniques for liquid foam. Adapting custom-tailored tracers for various foam bubble size and liquid fraction, the local velocity and also the vorticity are measurable directly with both high spatial and temporal resolution. To further the X-PTV technique and take advantage of the conical diverging X-ray beam, the tracer's position along the beam direction could be reconstructed from its apparent projected size, yielding three-dimensional trajectories.
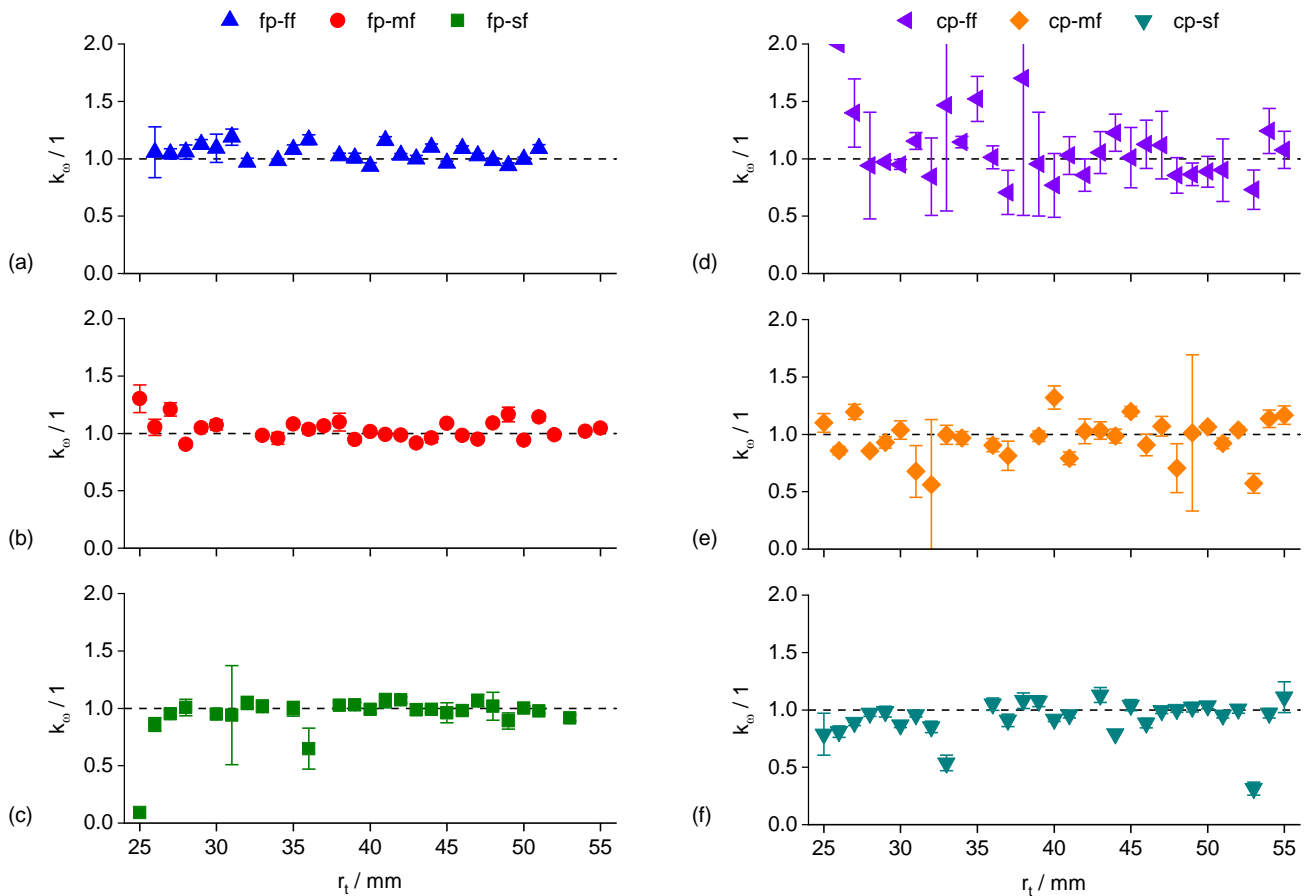
Fig. 12 Tracer translational motion and intrinsic rotation with (a)-(c) the fine-pored and (d)-(f) the coarse-pored foam flow in the semi-circular curved channel section: velocity ratio $k_\omega$, depending on the radius $r_t$.

## Conflicts of interest

There are no conflicts to declare.

## Acknowledgements

## References

1 S. Cohen-Addad, R. Höhler and O. Pitois, *Annual Review of Fluid Mechanics*, 2013, **45**, 241–267.

2 M. C. Fuerstenau and G. J. Jameson, *Froth flotation: a century of innovation*, Soc. for Mining, Metallurgy, and Exploration, Littleton, Colo, 2007.

3 B. Dollet, F. Elias, C. Quilliet, C. Raufaste, M. Aubouy and F. Graner, *Physical Review E*, 2005, **71**, 031403.

4 B. Dollet and F. Graner, *Journal of Fluid Mechanics*, 2007, **585**, 181–211.

5 S. Jones, B. Dollet, N. Slosse, Y. Jiang, S. Cox and F. Graner, *Colloids and Surfaces A: Physicochemical and Engineering Aspects*, 2011, **382**, 18–23.

6 K. Cole, P. Brito-Parada, C. Xu, S. Neethling and J. Cilliers, *Chemical Engineering Research and Design*, 2012, **90**, 2196–2201.

7 S. S. Park and D. J. Durian, *Physical Review Letters*, 1994, **72**, 3347–3350.

8 Y. Wang and S. J. Neethling, *Colloids and Surfaces A: Physicochemical and Engineering Aspects*, 2009, **339**, 73–81.

9 M. Asipauskas, M. Aubouy, J. A. Glazier, F. Graner and Y. Jiang, *Granular Matter*, 2003, **5**, 71–74.

10 S. Rodts, J. C. Baudez and P. Coussot, *Europhysics Letters*, 2005, **69**, 636–642.

11 R. Nauber, L. Büttner, K. Eckert, J. Fröhlich, J. Czarske and S. Heitkam, *Physical Review E*, 2018, **97**, 013113.

12 A. Buffler, K. Cole, T. Leadbeater and M. van Heerden, *International Journal of Modern Physics: Conference Series*, 2018, **48**, 1860113.

13 K. Cole, P. Brito-Parada, A. Morrison, I. Govender, A. Buffler, K. Hadler and J. Cilliers, *Chemical Engineering Research and Design*, 2015, **94**, 721–725.

14 S. Langford, C. Wiggins, D. Tenpenny and A. Ruggles, *Nuclear Engineering and Design*, 2016, **302**, 81–89.

15 C. Raufaste, B. Dollet, K. Mader, S. Santucci and R. Mokso, *Europhysics Letters*, 2015, **111**, 38004.

16 S. Heitkam, M. Rudolph, T. Lappan, M. Sarma, S. Eckert, P. Trtik, E. Lehmann, P. Vontobel and K. Eckert, *Minerals Engineering*, 2018, **119**, 126–129.

17  S. Heitkam, T. Lappan, S. Eckert, P. Trtik and K. Eckert, *Chemie Ingenieur Technik*, 2019, **91**, 1001–1007.

18  T. Dracos, *Three-Dimensional Velocity and Vorticity Measuring and Image Analysis Techniques*, Springer Netherlands, Dordrecht, 1996, vol. 4, pp. 155–160.

19  A. Dominguez, A. Fernandez, N. Gonzalez, E. Iglesias and L. Montenegro, *Journal of Chemical Education*, 1997, **74**, 1227.

20  K. J. Mysels, *Langmuir*, 1986, **2**, 423–428.

21  J. Hubbell and S. Seltzer, *Tables of X-Ray Mass Attenuation Coefficients and Mass Energy-Absorption Coefficients*, 2004, `http://physics.nist.gov/xaamdi`.

22  J.-Y. Tinevez, N. Perry, J. Schindelin, G. M. Hoopes, G. D. Reynolds, E. Laplantine, S. Y. Bednarek, S. L. Shorte and K. W. Eliceiri, *Methods*, 2017, **115**, 80–90.

23  S. J. Orfanidis, *Introduction to signal processing*, Prentice Hall, Englewood Cliffs, N.J, 1996.